Supplementary Information

Too Cool for Blackbody Radiation: Overbias Photon Emission in Ambient STM Due to Multi-Electron Processes

E-Dean Fung, Latha Venkataraman

S1. Coulomb Blockade Model

This section is organized as follows: We begin by simply restating our model to emphasize the physical units. We then relate it to the models developed by Tobiska and coworkers[1] and Xu and coworkers[2,3], which we will refer to as the Tobiska model and Xu model, respectively. Finally, we will compare it numerically to the Xu model.

The emission probability density, $P(E)$, is the probability of emitting a photon with energy in the interval $[E, E+dE]$ and has units of inverse energy (eV^{-1}). This is the probability of emission, not the probability of emission per electron. This is the sum of single and multi-electron processes as defined in the main text:

$$P(E) = P_{1e}(E) + P_{2e}(E) + P_{3e}(E) \dots$$

$$P_{1e}(E) = G_0 \widetilde{D}(E)\tilde{S}(E)$$

$$P_{2e}(E) = G_0^2 \widetilde{D}(E) \int_0^\infty d\varepsilon\, \widetilde{D}(\varepsilon)\tilde{S}(\varepsilon)\, \tilde{S}(E-\varepsilon)H(E-\varepsilon)$$

$$P_{3e}(E) = G_0^3 \widetilde{D}(E) \int_0^\infty d\varepsilon\, \widetilde{D}(\varepsilon)\tilde{S}(\varepsilon) \int_0^\infty d\varepsilon' \widetilde{D}(\varepsilon')\tilde{S}(\varepsilon') \cdot \tilde{S}(E-\varepsilon-\varepsilon')H(E-\varepsilon-\varepsilon')$$

We use the tilde to denote the non-normalized versions of $D(E)$ and $S(E)$, which are:

$$\tilde{S}(E) = G_0 \sum_n \left[2\tau_n^2 B(E) + \tau_n(1-\tau_n) \sum_{\pm} B(E \pm eV) \right]$$

$$\widetilde{D}(E) = \frac{\left|\tilde{Z}(E)\right|^2}{E^2}$$

$\tilde{Z}(E)$ is the complex impedance of the electromagnetic environment. This is typically modelled with an effective RLC circuit. To obtain the normalized version of these equations, we absorb two factors of G_0 into $\widetilde{D}(E)$. The normalized $D(E)$ is then defined as

$$D(E) = G_0^2 \widetilde{D}(E) = \frac{|Z(E)|^2}{E^2}$$

where $Z(E)$ is now the impedance normalized to the quantum of resistance i.e $Z(E) \equiv G_0 \tilde{Z}(E)$.

The Tobiska model[1] and Xu model[2,3] have an additional prefactor of $\frac{|\mathcal{T}|^2}{h}\alpha^2$, where $\mathcal{T}$ is the coupling between the two states of a quantum dot and α is the dimensionless coupling between the RLC circuit and the detector. This gives the emission rate with units of s^{-1}. We do not use a two-state quantum dot as a detector, so more generally, one can replace the constant $\mathcal{T}$ with $\mathcal{T}(E)$. We replace the entire prefactor $\frac{|\mathcal{T}|^2}{h}\alpha^2$ with $Q(E)$, for simplicity.

Both Tobiska and Xu provide a low temperature approximation for the two-electron process. However, this approximation is only valid between $1\ eV_{applied}$ and $2\ eV_{applied}$, i.e. the energy range where the two-

electron emission dominates. As mentioned in the main article and discussed in Ref. S3, there is significant mixing between processes of different orders at room temperature, which this approximation cannot capture. Rewriting the low temperature approximation using our notation and including the three-electron process from Peters *et al*, we get:[4]

$$P_{1e}(E) = D(E)S(E)$$

$$P_{2e}(E) = D(E)\int_{E-eV}^{eV} d\varepsilon\, D(\varepsilon)s(\varepsilon)\cdot s(E-\varepsilon)$$

$$P_{3e}(E) = D(E)\int_{E-2eV}^{eV} d\varepsilon\, D(\varepsilon)s(\varepsilon)\int_{E-eV-\varepsilon}^{eV} d\varepsilon' D(\varepsilon')s(\varepsilon')\cdot s(E-\varepsilon-\varepsilon')$$

Note that the current noise in the two- and three-electron process is not the full expression, but $s(E) = (eV-E)\sum_n \tau_n(1-\tau_n)$.

An analytical expression for the two-electron process at finite temperature was developed by Xu et al. However, we required in this work the three-electron process for comparison with the blackbody work. To achieve this, we simply extended the low temperature approximations above by using the full current noise expression, adjusting the limits of integration, and including a Heaviside function. This can be extended to n electrons: Each additional electron introduces an additional operator $\int d\varepsilon_i D(\varepsilon_i)S(\varepsilon_i)$, and the final electron energy becomes $E-\sum\varepsilon_i$. This last electron directly emits a total energy E, which is why the final factor of $D(E)$ is outside the integral.

In Figure S1, we compare our extended numerical approximation to the full analytical expression developed by Xu and coworkers. In Figure S1a, we simply use a featureless $D(E) = 0.1$ eV^{-2}. Since the complex and real parts of Z enter into the Xu model, we plot the result when $Z(E)$ is purely imaginary to correspond to the off-resonant case when a featureless $D(E)$ is a reasonable approximation. Our model is in excellent agreement with the Xu model, with some deviation below 1.0 eV.

We also compare the two models for a $D(E)$ with three resonances at 0.5, 1.5, and 2.5 eV. Again, we observe deviations below 1.0 eV. Since these calculations were done with an applied bias of 1 Volt, this simply means that our approximation is not valid in the underbias emission regime. But as the two-electron process only produces a small correction to the overall emission, our approximation is sufficient for the purposes of this work.

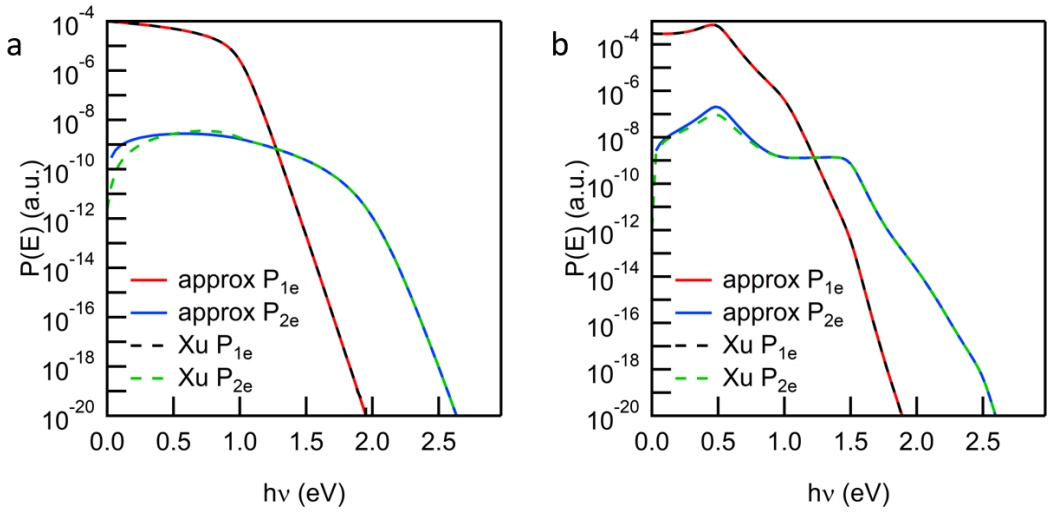

Figure S1: P_{1e} and P_{2e} calculated from our approximate model (red and blue, respectively) and the Xu model (black and green, respectively). (a) Using a featureless $D(E) = 0.1$ eV^{-2}. (b) Using three resonances as described in the Xu model, with resonances at 0.5, 1.5, and 2.5 eV and an effective broadening η of 0.2 eV for all three resonances. Other parameters: $\tau = 10^{-3}, T = 300$ K, $V_{applied} = 1.0$ V

S2. Reproducing Blackbody-like Phenomena

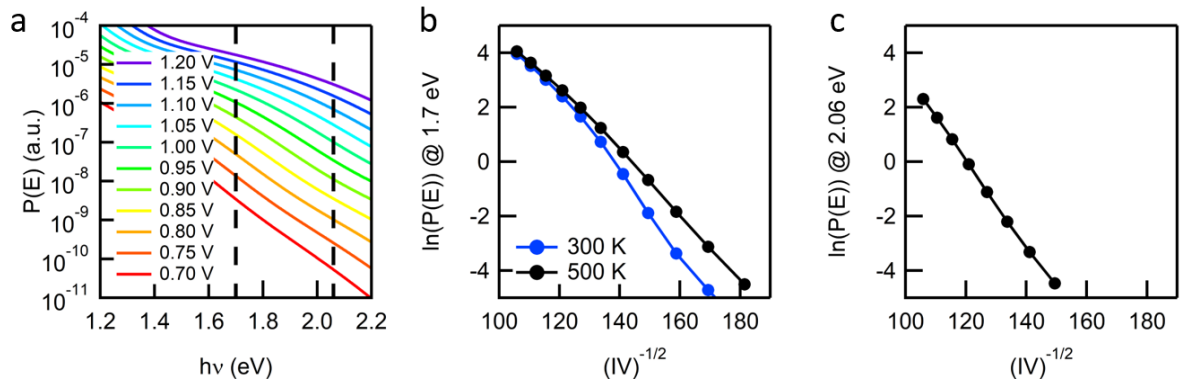

Figure S2: (a) Calculated total emission spectra $P(E) = P_{1e} + P_{2e} + P_{3e}$ for different applied voltage. Parameters: $D(E) = 0.1$ eV^{-2}, $\tau = 0.8$, $T = 500$ K. Vertical dashed lines at $h\nu = 1.7$ and 2.06 eV correspond to data used to produce (b) and (c), respectively. Figure S2b also includes the same calculation but at room temperature in blue. Note the vertical axis is the natural log. All curves in (b) and (c) are vertically shifted by the same amount to mimic values in Fig. 4 of Ref. S5.

We argue in the main manuscript that blackbody radiation cannot explain the superlinear dependence of emission on conductance observed here and in previous works. By contrast, we demonstrate here that emission from multi-electron processes can produce a dependence on electrical power very similar to that predicted by blackbody radiation. Specifically, we reproduce results in Refs. S5 and S6 that show $\ln(W) \propto 1/\sqrt{IV}$.

In Figure S2a, we plot the total emission probability density $P(E)$ including emission up to three-electron processes for a range of biases, using parameters corresponding to Ref. S5. The different spectra are roughly evenly spaced on a semi-log plot. By taking values at two different photon energies, we reproduce Figure 4 of Ref. S5 in Figures S2b,c here. Note that without assuming a temperature increase of 200 K, the trend deviates from $\ln(W) \propto 1/\sqrt{IV}$.

Next, we reproduce Figure 2b from Ref. S6, which we will refer to as Downes 2002. This calculation is slightly more involved. First, Fig. 2b in Downes 2002 is the detected photon rate, not the emitted photon rate.[7] Second, the detected photons are over a broad range of frequencies, dictated by the quantum efficiency of the detector used. This is provided in Fig. 4.9 of Ref. S8. Third, close inspection of Fig. 2a in Downes 2002 shows that the conductance and the applied voltage are correlated. At room temperature, the large electric fields can cause the Au atoms to shift closer together, increasing the conductance. By assuming a linear relationship between conductance and voltage, we qualitatively reproduce Fig. 2b in Downes 2002 using our model in Figure S3a.

Downes *et al* also repeated the measurement with a bandpass filter. This is provided in Fig. 7.13 of Ref. S8. Assuming a fixed conductance of 0.4 G_0 is sufficient to reproduce the trend. Figure S3b shows the results from our calculation, in excellent agreement with their measurement.

At fixed bias, the emission predicted by blackbody radiation is approximately exponential for $E \gg k_B T$, as depicted in Figure 3 of Downes 2002. This, too, can be reproduced by emission from multi-electron processes. In Figure S3c, we calculate the emission spectra at fixed bias using the parameters in Ref. S6. If

we assume again an elevated electronic temperature of 500 K, the total emission spectra is roughly exponential. These comparisons indicate that the results of Refs. S5 and S6 can be explained without having to invoke extreme electronic temperatures.

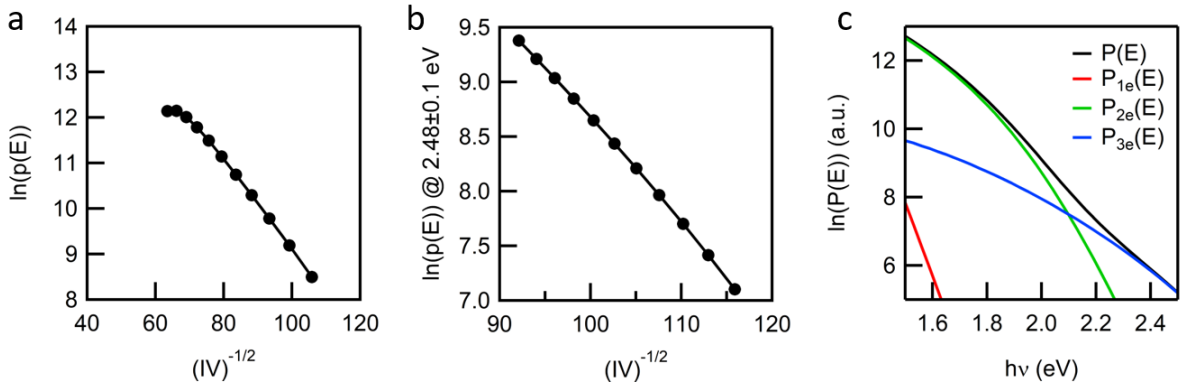

Figure S3: (a) Spectrum $p(E)$ integrated across all wavelengths for voltages between 1.2 and 2.0, plotted against $(IV)^{-0.5}$. Compare with Fig. 2b of Ref. S6. Parameters: $D(E) = 0.1$ eV^{-2}, $\tau = 0.7 - 0.95$, $T = 500$ K. (b) Spectrum $p(E)$ integrated between 2.38-2.58 eV for voltages between 1.55 and 1.95, plotted against $(IV)^{-0.5}$. Compare with Fig. 7.13 of Ref. S8. Parameters: $D(E) = 0.1$ eV^{-2}, $\tau = 0.4$, $T = 500$ K. (c) Total emission (black) as a function of photon energy, with contributions from 1e, 2e, and 3e processes in red, green, and blue, respectively. Compare with Fig.3 of Ref. S6. Parameters: $D(E) = 0.1$ eV^{-2}, $\tau = 1.3$, $T = 500$ K, $V_{applied} = 1.0$ V. All curves vertically shifted to mimic published results.

S3. Comparison of Blackbody Radiation and Emission from Inelastic Processes

Hone *et al.* provided an expression for the total power radiated from inelastic tunneling[9]

$$W = \frac{\pi e^2}{\hbar c \varepsilon_0}\left(\frac{aeV}{hc}\right)^2 IV$$

where a is the effective radius of the tip. For a conductance of 0.1 G_0, a bias of 1.4 V, and an effective radius of $\sim$100 nm, this is approximately 50 nW.

The maximum photovoltage without filters we measure ranges between 0.03 V and 0.3 V. From our spectra, we know that the majority of the light has wavelength greater than 700 nm, where the detector responsivity is less than 0.5 V/nW. If we estimate the fraction of photons detected to be $\sin^{-1}(NA)/\pi \approx 30\%$ (NA is the numerical aperture of the objective lens), the total power measured is between 0.2 and 10 nW, in reasonable agreement with the estimate from the expression from Hone *et al*. We note the experiment underestimates of the total emitted power, since a significant proportion of the emitted power is in the NIR, which we do not measure.

Assuming the vacuum local density of states, the emitted blackbody radiation from an area A is[10]

$$\frac{W}{A} = \frac{\pi^2}{60}\frac{1}{c^2\hbar^3}(k_B T)^4$$

Assuming $A\sim10^3$ nm^2, the total power radiated for $T = 500$ and 2000 K is 0.03 pW and 0.1 nW, respectively. The contribution from low temperature electrons can be safely neglected, and we argue that the emission from a hypothetical electronic temperature of 2000 K is too small to account for our experimental observations. It is only consistent with the lower end of our experimental values, which is already an underestimate of the total power. We have estimated the area based on the scale of the electron-phonon mean free path (~30 nm).[11,12]

The estimates above are lacking in two respects. First, they do not fairly compare the effect of surface plasmons. Second, they only provide an analysis of the total power and not the spectral dependence. There may exist a cross-over region where blackbody radiation exceeds emission from inelastic tunneling.

To theoretically compare blackbody radiation and emission from multi-electron processes, we must choose a unifying framework. We will approach the problem from the perspective of statistical mechanics. The cross spectral density of the electric field can be written in terms of the electric Green's function and the cross spectral density of the current density.[13]

$$\langle E_k(\boldsymbol{r},\omega)E_l^*(\boldsymbol{r}',\omega')\rangle = \langle \mu_0^2\omega^2 \int d^3\boldsymbol{r}_1 d^3\boldsymbol{r}_2 G_{km}^{EE}(\boldsymbol{r},\boldsymbol{r}_1,\omega)\, j_m(\boldsymbol{r}_1,\omega) j_n^*(\boldsymbol{r}_2,\omega') G_{ln}^{EE^*}(\boldsymbol{r}',\boldsymbol{r}_2,\omega)\rangle$$

For a local and isotropic material, we obtain

$$\langle E_k(\boldsymbol{r},\omega)E_l^*(\boldsymbol{r}',\omega')\rangle = \mu_0^2\omega^2 \int d^3\boldsymbol{r}_1 \langle j_m(\boldsymbol{r_1},\omega) j_n^*(\boldsymbol{r_1},\omega')\rangle G_{km}^{EE}(\boldsymbol{r},\boldsymbol{r}_1,\omega)\, G_{ln}^{EE^*}(\boldsymbol{r}',\boldsymbol{r}_1,\omega) \qquad (S1)$$

where $\boldsymbol{r}_1$ ranges over the space of current fluctuation sources. The Green's function contains information of the density of states (found in the expression for blackbody radiation) and the

electromagnetic impedance (which is found in $D(E)$ in the model for multi-electron processes).[14–16] We will ignore the effect of the Green's function and isolate the problem to comparing the current density fluctuations $\langle j_m(\omega) j_n^*(\omega')\rangle$.

The current fluctuations in a bulk material which give rise to blackbody radiation is given by[13,17,18]

$$\langle j_m(\boldsymbol{r},\omega) j_n^*(\boldsymbol{r}',\omega')\rangle = \frac{\omega}{\pi}\varepsilon_0\varepsilon''(\omega)\delta_{mn}\delta(\omega-\omega')\delta(\boldsymbol{r}-\boldsymbol{r}')\frac{\hbar\omega}{e^{\frac{\hbar\omega}{k_BT}}-1} \qquad (S2)$$

where ε_0 is the vacuum permittivity and ε'' is the imaginary part of the dielectric constant.

The current fluctuations due to tunneling is given by $\tilde{S}(\omega)$

$$\tilde{S}(\omega) = \langle I(\omega) I(\omega')\rangle = \delta(\omega-\omega')G_0\sum_n\left[2\tau_n^2 B(\hbar\omega) + \tau_n(1-\tau_n)\sum_{\pm} B(\hbar\omega \pm eV)\right]$$

$$B(\hbar\omega) = \frac{\hbar\omega}{e^{\hbar\omega/k_BT}-1}$$

To convert $\tilde{S}(\omega)$ into $\langle j(\boldsymbol{r},\omega) j^*(\boldsymbol{r}',\omega')\rangle$, we consider the current fluctuations in the tunnel junctions as a point-dipole such that

$$\langle j(\boldsymbol{r},\omega) j^*(\boldsymbol{r}',\omega')\rangle = \frac{\tilde{S}(\omega)}{d}\delta(\omega-\omega')\delta(\boldsymbol{r}-\boldsymbol{r}') \qquad (S3)$$

where d is the tunnel gap distance.

We plot Eq. S2 for two temperatures (assuming $\varepsilon'' = 1$) and Eq. S3 for two voltages (assuming $\tau = 0.1, T = 500$ K, $d = 1$ nm) in Figure S4. For the same temperature, the emission from inelastic tunneling dominates at all photon energies. For blackbody radiation at an elevated temperature, the crossover region depends on the bias. Note that this calculation only considers the emission from 1e processes and does not include multi-electron processes, which would increase the emission for larger photon energies. This could push the crossover to higher photon energies depending on the magnitude of the emission from 2e processes. Finally, the relative strengths of current noise from inelastic tunneling and blackbody radiation in Figure S4 are in good agreement with the relative magnitude of the total power presented in the beginning of this section.

Let us briefly consider the effect of the remaining parameters. ε'' is large for MIR photons (as large as 10^4), so blackbody radiation may be comparable to emission from inelastic tunneling at long wavelengths. For wavelengths in the visible spectrum (where most experiments are performed), ε'' is only around 10 at most.[19] The plasmonic enhancement should be strongest in the tunnel junction, which could increase the ratio between emission from inelastic tunneling and blackbody radiation, but the integral in Eq. S1 covers a larger volume in the case of blackbody radiation. We do not expect this to substantially increase blackbody radiation relative to emission from inelastic tunneling.

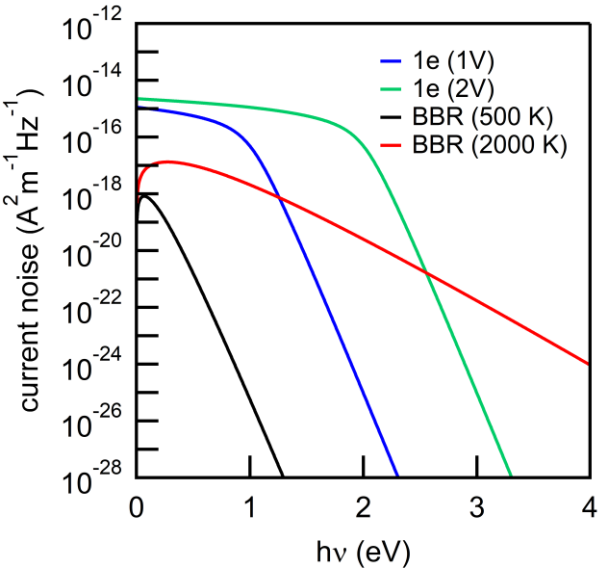

Figure S4: The current noise from blackbody radiation at two temperatures and the 1e emission from a junction with $\tau = 0.1$, $T = 500$ K, and $d = 1$ nm at two biases. We drop the units in the Dirac-delta functions.

S4. Experimental Setup

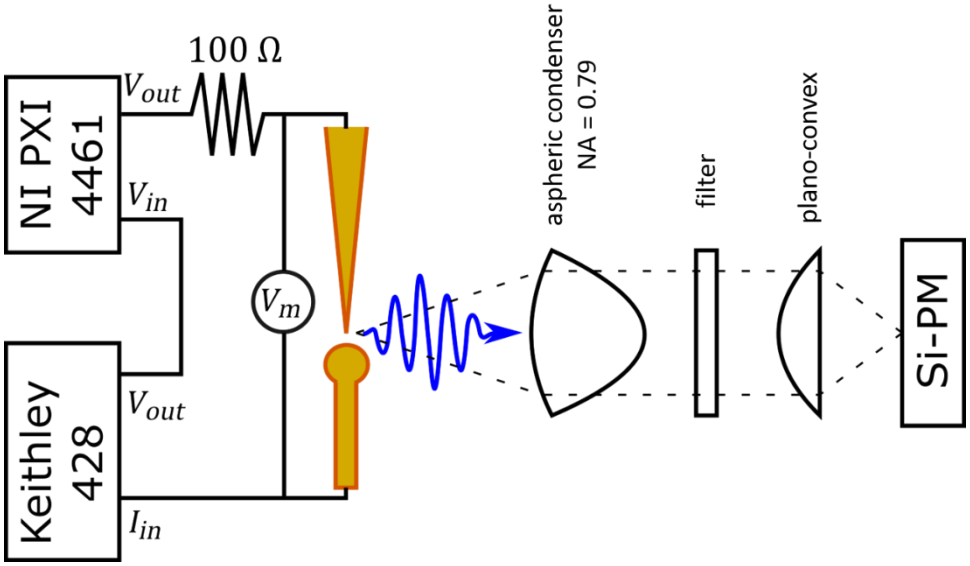

Figure S5: Schematic of experimental setup

Figure S5 is a schematic of the modified STM. Note that we measure the voltage drop across the tunnel junction (V_m), i.e. not including the voltage drop across the 100 Ω resistor. The conductance is then calculated as $G = I/V_m$ in units of G_0. The measured voltage is less than the applied voltage, but the difference is only about 1% of the applied voltage for conductances around G_0 and much less for lower conductances.

All optical filters are purchased from Thorlabs. The part numbers are:

Bandpass Filters: FKB-VIS-10, FL850-10, FB900-10, FB950-10, FB1000-10

Edgepass filters: FESH0750, FELH0750

S5. Data Analysis

Before any analysis, we subtract the average background signal in the photovoltage and apply an 101 point boxcar smoothing (rolling average) to help distinguish signal from noise. The width of the moving average is justified by considering the length and time scales of the relevant physics. We are interested in the dependence on the log-conductance, which depends linearly on the displacement. We are only interested in angstrom-scale displacements as opposed to sub-angstrom thermal fluctuations. Our push rate is approximately 20 nm/s. With an acquisition rate of 100 kHz, angstrom-scale displacements correspond to 500 points. The width of our moving average is well within this limit.

The 2D photovoltage-conductance histograms are constructed from the smoothed data during the segment when a high bias is applied (shaded region in Fig. 1a in main manuscript). Some traces will not display electroluminescence in this region because either the efficiency or conductance is low. Unless noted otherwise, the 2D histograms are constructed without selection.

Depending on the experiment, there are between 15,000 to 30,000 points during the high bias hold. Hence, a 4σ event, corresponding to approximately 1 in 30,000 events, is a reasonable threshold to separate signal from noise. The sample standard deviation is calculated from the smoothed data.

S6. Spectra

The spectra are produced by collecting 1000 traces at each wavelength window (600 – 1000 nm, 50nm spacing, $\sim$10 nm FWHM). For each trace, we calculate the mean photovoltage of the points that are (A) 4σ above noise and (B) between 0.9 and 1.1 G_0. Finally, we average the mean photovoltage of each trace, ignoring traces that do not show any signal, to generate a representative photovoltage at each wavelength.

Figure S6 shows the 2D photovoltage-conductance histograms for the nine different wavelengths measured. The black dot in each histogram represents the representative photovoltage extracted by the algorithm above and depicted in Fig. 1d of the main manuscript.

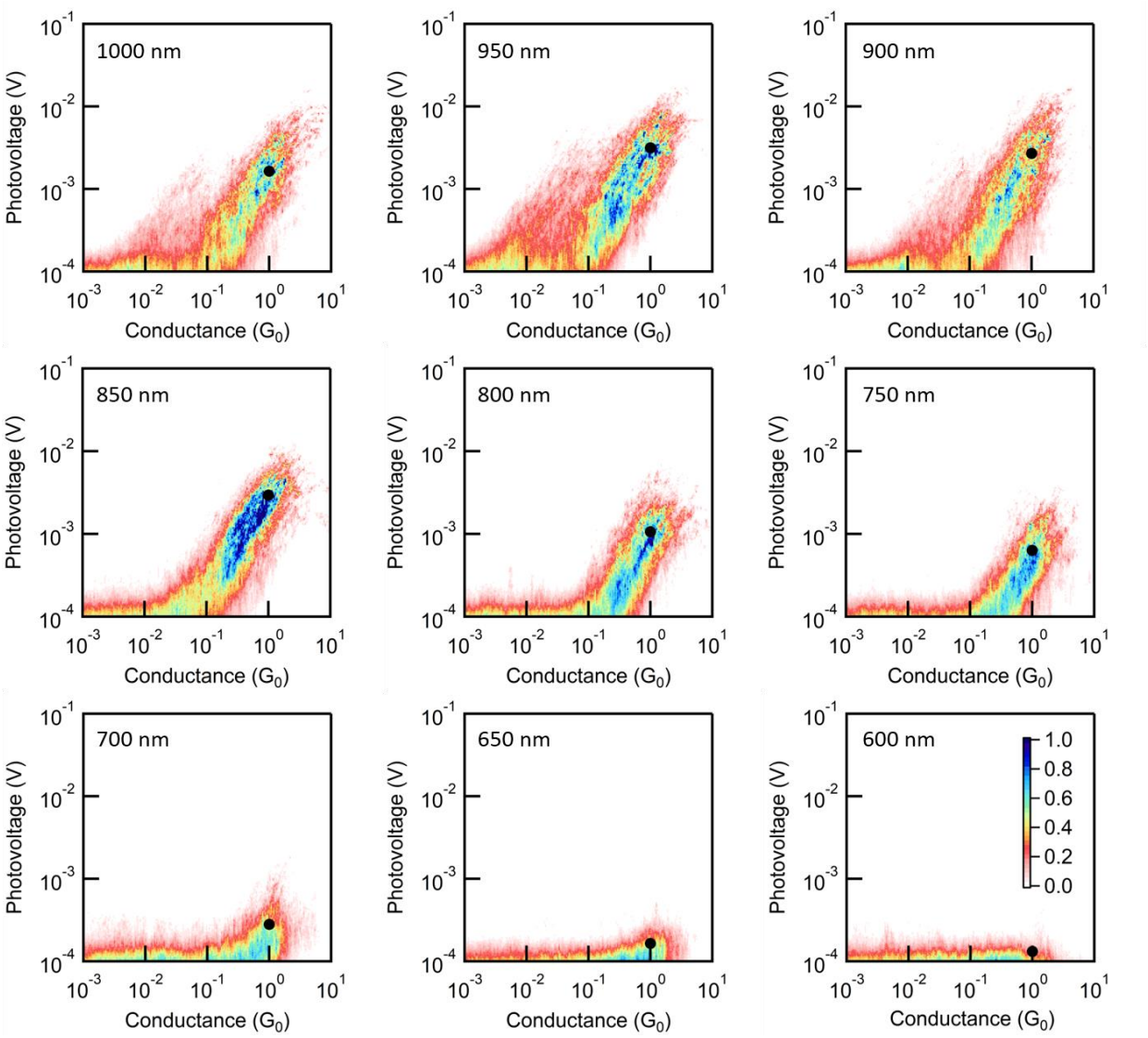

Figure S6: 2D histograms corresponding to the spectrum in Figure 1d of the main manuscript. The black dots in each histogram correspond to the points in Fig. 1d.

S7. Superlinear Analysis

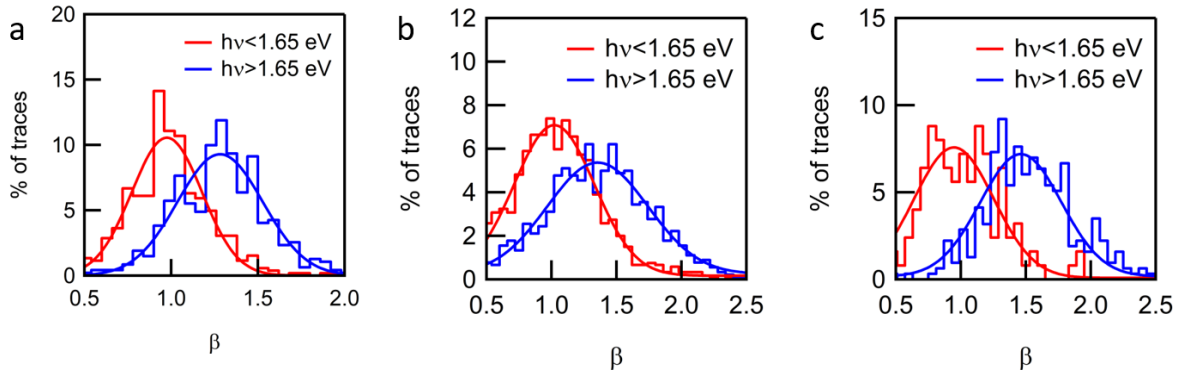

Figure S7: (a) Histograms of the fitted β, corresponding to Fig. 3b,c (red and blue, respectively). Histograms of the fitted β from two separate experiment performed at applied bias of (b) 1.4 V and (c) 1.65 V. Same filters (cutoff wavelength 750 nm) are used throughout.

To characterize the variability between tunnel junctions, we fit the data from junctions that show clear emission to a power law, i.e. $V_{photo} \propto G^{\beta}$. As explained in the main manuscript, there are two types of junctions measured: higher efficiency junctions that we hypothesize are pristine tunnel junctions, and lower efficiency but higher conducting junctions that we hypothesize contain a water bridge. Only the second junction is visible with a lowpass filter. Since there is some overlap between the conductances of the two types of junctions (see Fig. 1c in the main manuscript), we only fit points with conductances between 0.1 and 10 G_0. This means we only consider water tunnel junctions. We only consider points 4σ above noise when fitting.

The fitted β values are then compiled into the β histograms in Figure S7a. Surprisingly, there is considerable variability in β for both the underbias and overbias emission. We hypothesize that the changes in tip geometry from junction to junction explains this variance. In the tunneling regime, the electric field enhancement decreases and the surface plasmon modes blue-shift as the junction gap decreases.[20–23] These two trends have opposing effects: a decrease in field enhancement decreases β, whereas a blue-shift in the surface plasmon modes, which for cut-tips will lie in the near-infrared, could increase β. In addition, the charge transfer plasmons are extremely important in the tunneling regime and are quite sensitive to the local geometry.[24–27] The break-junction methodology samples many tip geometries that may result in superlinear or sublinear β. In Eq. 1-3, these effects can be modeled by a $D(E)$ that depends on the transmission coefficient τ (see Section S8).

To demonstrate the repeatability of the superlinear relation between emission and conductance in the overbias regime, we show in Figure S7b,c the same phenomenon with two different tips and two different biases. The shift in mean fitted β between the underbias and overbias emission is comparable in all cases. The inability to obtain a β approaching 2 even when the shortpass filter cutoff energy is higher than the energy supplied bias the bias is likely a limitation of the sensitivity of the detector.

We rule out two other explanations for the observed variance in β. First, we argue that this variance is not due to the water in the junction. Figure S8a shows the 2D histogram showing only pristine tunnel junctions and no water tunnel junctions due to the application of a 2 kΩ resistor. Figure S8b is the

corresponding histogram for the fitted β. We observe a similar variance as with experiments performed with a 100 Ω resistor. This means that the variance is not a feature of the water tunnel junctions.

Second, we argue that this variance is not a result of error in the fitting. Figures S8c and S8d are two traces with the corresponding fit in red.

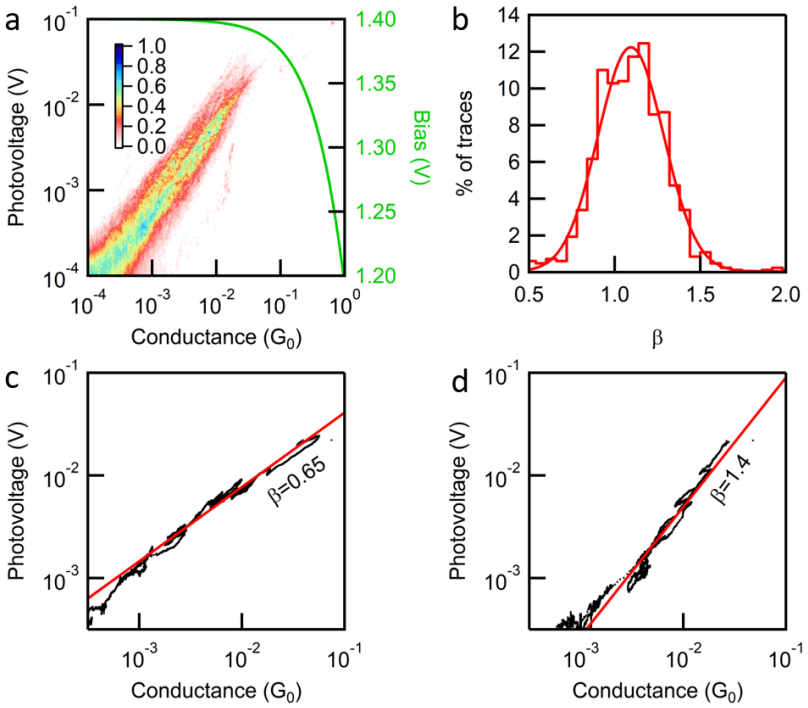

Figure S8: (a) 2D histogram of photovoltage vs conductance for experiment performed with 2 kΩ resistor (see Fig. S5) and without any optical filter. Theoretical junction bias overlaid in green. Note that the second lobe corresponding to water tunnel junctions seen in Figure 1c of the main manuscript is absent here. This because at conductances above 10^{-2} G_0, the applied bias begins to drop across the series resistor instead of the tunnel junction. This suppresses the current, along with the light emission. (b) Histogram of β values extracted from traces in (a). Junctions with (c) sublinear and (d) superlinear β.

S8. The Role of $D(E)$

We will limit our discussion to featureless $D(E)$, i.e. independent of photon energy. First, we justify our choice of $D(E) = 0.1$ eV^{-2}. When $D(E)$ is constant, its role is primarily to regulate the relative intensities of the different orders of multi-electron emission. Specifically, larger $D(E)$ results in a larger two-electron emission relative to the one-electron emission. The relative strengths of emission of different orders was measured by Peters and coworkers and is provided in Figure 3a of Ref. 4. We qualitatively reproduce their experiment in Figure S9a using our chosen parameter of $D(E) = 0.1$ eV^{-2}.

Next, we further justify the chosen temperature increase of 200 K. The calculation in Figure S9a is not very sensitive to temperature; a lower temperature will provide similar agreement. However, the β of 1.7 reported in Ref. S28 requires a fairly substantial temperature increase. Assuming $D(E) = 0.1$ eV^{-2}, ΔT should be approximately 200 K to fit both the β value reported in Ref. S28 and the β measured in this work. Figure S9b is the calculated conductance dependence for parameters in Ref. S28.

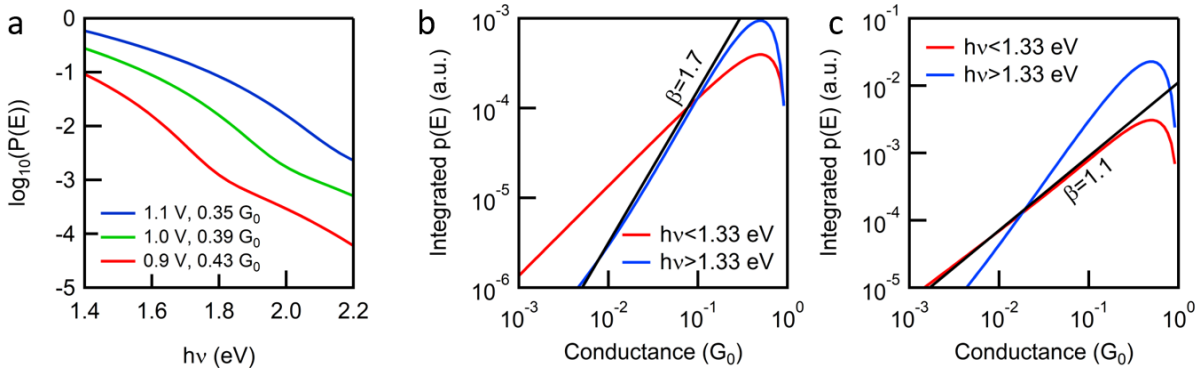

Figure S9: (a) Normalized emission spectra simulating Fig. 3a in Ref. S4. Parameters: $D(E) = 0.1$ eV^{-2}, $T = 200$ K. (b) Integrated $P(E)$ showing $\beta = 1.7$ in overbias emission. Parameters: $D(E) = 0.1$ eV^{-2}, $T = 200$ K, $V_{applied} = 1.33$ V. (c) Same parameters as (b) except $D(E) = 0.5$ eV^{-2}, showing slightly superlinear dependence of underbias emission.

A different choice of $D(E)$ will require a different temperature in order to produce the correct β in the overbias emission. Specifically, as $D(E)$ increases, so does the required temperature. One might be concerned that this makes it impossible to estimate the temperature without a precise measure of $D(E)$. Worse, if $D(E)$ is arbitrarily large, the temperature can also be arbitrarily large and the argument that blackbody radiation and multi-electron processes are incompatible would no longer hold.

However, $D(E)$ cannot consistently exceed $\sim 1/\tau$ across all wavelengths, otherwise the theory will predict more two-electron emission than one-electron emission. Since we sample conductance around 0.1 G_0, $D(E)$ should be less than 10 eV^{-2}.

A tighter bound is obtained by observing that although the underbias emission does display some superlinear dependence, it is only around $\beta = 1.1$ on average. The superlinear dependence of underbias emission is not very sensitive to temperature (unlike the overbias emission), so we can use this value to estimate $D(E)$ independent of temperature. We find a $D(E) \sim 0.5$ eV^{-2} corresponds well to a $\beta = 1.1$ in the underbias emission. Figure S9c shows the result for a calculation using the parameters in Ref. S28. The

main result of this analysis is that $D(E)$ is somewhere between 0.1 and 0.5 eV^{-2}. Temperatures of 2000 K are inconsistent with this range of $D(E)$.

We use $D(E) = 0.1$ eV^{-2} because a lower value fits a wider range of experiments. An elevated $D(E)$ in the NIR is easily explained by the presence of surface plasmon resonances in the NIR. In other words, it is sufficient to assume that $D(E)\sim 0.5$ eV^{-2} for photon energies in the underbias regime to obtain $\beta = 1.1$ for underbias emission. We need not assume $D(E)\sim 0.5$ eV^{-2} across the entire spectrum. See Section S9.

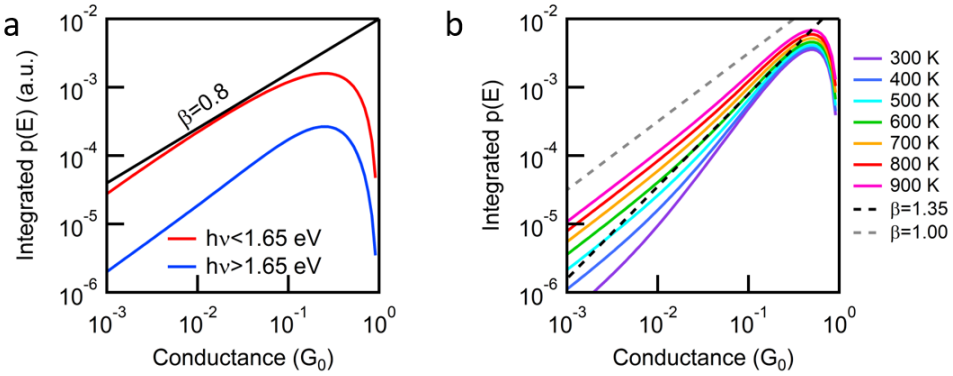

Figure S10: (a) Same parameters as Fig. 3c in the main manuscript except with conductance dependent $D(E)$, resulting in consistent sublinear trend. (b) Integrated spectra for overbias emission. Same parameters as Fig. 3d in the main manuscript except with different temperatures.

We hypothesize that the variance in β is best explained by the gap dependence of the surface plasmon resonances, which causes a correlation between conductance and $D(E)$. To demonstrate this, we model the decrease in electric field enhancement with a simple quadratic function $D(E,\tau) = \frac{0.1}{16}\log(\tau)\,(\log(\tau)+8)$. The resulting sublinear conductance dependence in plotted in Figure S10a. Superlinear conductance in both the underbias emission and overbias emission can be explained with a $D(E)$ that increases as a function of conductance or simply a larger value for $D(E)$.

Finally, we verify that the measured β is not compatible with higher temperatures. In Figure S10b, we plot the theoretical conductance dependence of the overbias emission for different temperatures. A temperature of 600 K is still consistent with $\beta = 1.35$, but by 900 K the β is very close to linear.

S9. The Energy Dependence of $D(E)$

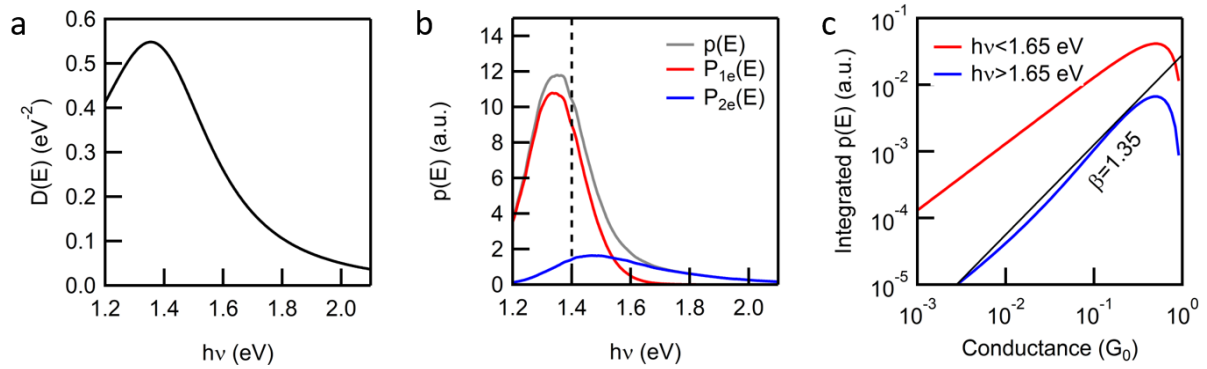

Figure S11: (a) $D(E)$ using parameters: $C = 0.1$ aF, $\hbar\omega_0 = 1.4$ eV, $\hbar\eta = 0.5$ eV. (b) $p(E)$ using $T = 500$ K, $\tau = 0.1$, and $D(E)$ in (a). (c) $p(E)$ spectrum for a range of conductances integrated over the underbias (red) and overbias (blue) regimes. The slope is preserved under the energy-dependent $D(E)$.

We have assumed a flat $D(E)$ throughout this study. In this section, we will relax this assumption and investigate how it affects the claims in the manuscript.

First, we compare the experimental spectra in Fig. 1d and with the theoretical spectrum in Fig. 2d. The first major difference is that whereas the theoretical spectrum has a very long tail due to the 2e emission, both experimental spectra do not show any emission past 2 eV. This is likely due to the fact that there are plasmonic resonances in the NIR for cut tips but not in the visible. We can model this using a single plasmon mode.[2,3]

$$D(E) = \left(\frac{|Z|}{E}\right)^2$$

$$\tilde{Z}_\omega = i\sqrt{\frac{L}{C}}\frac{\omega_0\omega}{\omega_0^2 - \omega^2 + i\omega\eta} \qquad \omega_0 = \frac{1}{\sqrt{LC}} \qquad \eta = RC$$

$$\frac{Z(E)}{E} = \frac{G_0\tilde{Z}(E)}{E} = i\frac{\hbar G_0}{C}\frac{1}{(\hbar\omega_0)^2 - E^2 + iE\hbar\eta}$$

We find the following parameters qualitatively reproduce our spectra $C = 0.1$ aF, $\hbar\omega_0 = 1.4$ eV, $\hbar\eta = 0.5$ eV. The resulting $D(E)$, theoretical spectrum, and conductance dependence is shown in Figure S11. Importantly, we see that the conductance dependence is preserved under this analysis.

The second major discrepancy between theory and experiment is the presence of a double peak in the measurement performed at 1.4 V. Although in principle this can also be explained with an energy dependent $D(E)$, we note that each point in the spectra collected via the break-junction method takes approximately thirty minutes to collect and can be sensitive to changes over time. In addition, the bandpass filter at 1.46 eV (corresponding to the second "peak") has a ~20% higher peak transmission probability according to the manufacturer. There is some risk of over-interpreting features in the spectra.

Finally, a non-constant $D(E)$ has no impact on the ability of the theory to reproduce the $\ln\left(W_{BBR}(E)\right) \propto -(\alpha IV)^{-0.5}$ trend. This is because this trend is analyzed at a single wavelength. $D(E)$ will only scale the result, which amounts to a vertical shift on a semi-log plot. The trend will be identical, otherwise.

References

(1) Tobiska, J.; Danon, J.; Snyman, I.; Nazarov, Yu. V. Quantum Tunneling Detection of Two-Photon and Two-Electron Processes. *Phys. Rev. Lett.* **2006**, *96* (9), 096801. https://doi.org/10.1103/PhysRevLett.96.096801.

(2) Xu, F.; Holmqvist, C.; Belzig, W. Overbias Light Emission Due to Higher-Order Quantum Noise in a Tunnel Junction. *Phys. Rev. Lett.* **2014**, *113* (6), 066801. https://doi.org/10.1103/PhysRevLett.113.066801.

(3) Xu, F.; Holmqvist, C.; Rastelli, G.; Belzig, W. Dynamical Coulomb Blockade Theory of Plasmon-Mediated Light Emission from a Tunnel Junction. *Phys. Rev. B* **2016**, *94* (24), 245111. https://doi.org/10.1103/PhysRevB.94.245111.

(4) Peters, P.-J.; Xu, F.; Kaasbjerg, K.; Rastelli, G.; Belzig, W.; Berndt, R. Quantum Coherent Multielectron Processes in an Atomic Scale Contact. *Phys. Rev. Lett.* **2017**, *119* (6), 066803. https://doi.org/10.1103/PhysRevLett.119.066803.

(5) Buret, M.; Uskov, A. V.; Dellinger, J.; Cazier, N.; Mennemanteuil, M.-M.; Berthelot, J.; Smetanin, I. V.; Protsenko, I. E.; Colas-des-Francs, G.; Bouhelier, A. Spontaneous Hot-Electron Light Emission from Electron-Fed Optical Antennas. *Nano Lett.* **2015**, *15* (9), 5811–5818. https://doi.org/10.1021/acs.nanolett.5b01861.

(6) Downes, A.; Dumas, Ph.; Welland, M. E. Measurement of High Electron Temperatures in Single Atom Metal Point Contacts by Light Emission. *Appl. Phys. Lett.* **2002**, *81* (7), 1252–1254. https://doi.org/10.1063/1.1497188.

(7) Downes, A. University of Edinburgh, Personal Communication, 2020.

(8) Downes, A. R. Photon Emission from Metals in the Scanning Tunnelling Microscope. Ph.D. Dissertation, University of Cambridge, 1997.

(9) Hone, D.; Mühlschlegel, B.; Scalapino, D. J. Theory of Light Emission from Small Particle Tunnel Junctions. *Appl. Phys. Lett.* **1978**, *33* (2), 203–204. https://doi.org/10.1063/1.90275.

(10) Reif, F. *Fundamentals of Statistical and Thermal Physics*; Waveland Press: Long Grove, IL, 2009.

(11) Sze, S. M.; Moll, J. L.; Sugano, T. Range-Energy Relation of Hot Electrons in Gold. *Solid-State Electronics* **1964**, *7* (7), 509–523. https://doi.org/10.1016/0038-1101(64)90088-7.

(12) Kanter, H. Slow-Electron Mean Free Paths in Aluminum, Silver, and Gold. *Phys. Rev. B* **1970**, *1* (2), 522–536. https://doi.org/10.1103/PhysRevB.1.522.

(13) Joulain, K.; Mulet, J.-P.; Marquier, F.; Carminati, R.; Greffet, J.-J. Surface Electromagnetic Waves Thermally Excited: Radiative Heat Transfer, Coherence Properties and Casimir Forces Revisited in the near Field. *Surface Science Reports* **2005**, *57* (3), 59–112. https://doi.org/10.1016/j.surfrep.2004.12.002.

(14) Joulain, K.; Carminati, R.; Mulet, J.-P.; Greffet, J.-J. Definition and Measurement of the Local Density of Electromagnetic States Close to an Interface. *Phys. Rev. B* **2003**, *68* (24), 245405. https://doi.org/10.1103/PhysRevB.68.245405.

(15) Greffet, J.-J.; Laroche, M.; Marquier, F. Impedance of a Nanoantenna and a Single Quantum Emitter. *Phys. Rev. Lett.* **2010**, *105* (11), 117701. https://doi.org/10.1103/PhysRevLett.105.117701.

(16) Carminati, R.; Cazé, A.; Cao, D.; Peragut, F.; Krachmalnicoff, V.; Pierrat, R.; De Wilde, Y. Electromagnetic Density of States in Complex Plasmonic Systems. *Surface Science Reports* **2015**, *70* (1), 1–41. https://doi.org/10.1016/j.surfrep.2014.11.001.
(17) Carminati, R.; Greffet, J.-J. Near-Field Effects in Spatial Coherence of Thermal Sources. *Phys. Rev. Lett.* **1999**, *82* (8), 1660–1663. https://doi.org/10.1103/PhysRevLett.82.1660.
(18) Shchegrov, A. V.; Joulain, K.; Carminati, R.; Greffet, J.-J. Near-Field Spectral Effects Due to Electromagnetic Surface Excitations. *Phys. Rev. Lett.* **2000**, *85* (7), 1548–1551. https://doi.org/10.1103/PhysRevLett.85.1548.
(19) Olmon, R. L.; Slovick, B.; Johnson, T. W.; Shelton, D.; Oh, S.-H.; Boreman, G. D.; Raschke, M. B. Optical Dielectric Function of Gold. *Phys. Rev. B* **2012**, *86* (23), 235147. https://doi.org/10.1103/PhysRevB.86.235147.
(20) Esteban, R.; Borisov, A. G.; Nordlander, P.; Aizpurua, J. Bridging Quantum and Classical Plasmonics with a Quantum-Corrected Model. *Nature Communications* **2012**, *3*, 825. https://doi.org/10.1038/ncomms1806.
(21) Kravtsov, V.; Berweger, S.; Atkin, J. M.; Raschke, M. B. Control of Plasmon Emission and Dynamics at the Transition from Classical to Quantum Coupling. *Nano Lett.* **2014**, *14* (9), 5270–5275. https://doi.org/10.1021/nl502297t.
(22) Marinica, D. C.; Kazansky, A. K.; Nordlander, P.; Aizpurua, J.; Borisov, A. G. Quantum Plasmonics: Nonlinear Effects in the Field Enhancement of a Plasmonic Nanoparticle Dimer. *Nano Lett.* **2012**, *12* (3), 1333–1339. https://doi.org/10.1021/nl300269c.
(23) Zuloaga, J.; Prodan, E.; Nordlander, P. Quantum Description of the Plasmon Resonances of a Nanoparticle Dimer. *Nano Lett.* **2009**, *9* (2), 887–891. https://doi.org/10.1021/nl803811g.
(24) Savage, K. J.; Hawkeye, M. M.; Esteban, R.; Borisov, A. G.; Aizpurua, J.; Baumberg, J. J. Revealing the Quantum Regime in Tunnelling Plasmonics. *Nature* **2012**, *491* (7425), 574–577. https://doi.org/10.1038/nature11653.
(25) Koya, A. N.; Lin, J. Charge Transfer Plasmons: Recent Theoretical and Experimental Developments. *Applied Physics Reviews* **2017**, *4* (2), 021104. https://doi.org/10.1063/1.4982890.
(26) Halas, N. J.; Lal, S.; Chang, W.-S.; Link, S.; Nordlander, P. Plasmons in Strongly Coupled Metallic Nanostructures. *Chem. Rev.* **2011**, *111* (6), 3913–3961. https://doi.org/10.1021/cr200061k.
(27) Jiang, N.; Zhuo, X.; Wang, J. Active Plasmonics: Principles, Structures, and Applications. *Chem. Rev.* **2018**, *118* (6), 3054–3099. https://doi.org/10.1021/acs.chemrev.7b00252.
(28) Schull, G.; Néel, N.; Johansson, P.; Berndt, R. Electron-Plasmon and Electron-Electron Interactions at a Single Atom Contact. *Phys. Rev. Lett.* **2009**, *102* (5), 057401. https://doi.org/10.1103/PhysRevLett.102.057401.